Geophysical Journal International

Geophys. J. Int. (2023) **234,** 1024–1031
Advance Access publication 2023 March 11
GJI Rock and Mineral Physics, Rheology

https://doi.org/10.1093/gji/ggad100

Mapping faults in the laboratory with seismic scattering 2: the modelling perspective

Thomas King,[1,2] Luca De Siena,[3,4] Yi Zhang,[3] Nori Nakata,[5] Philip Benson[6] and Sergio Vinciguerra[2]

[1]*National Buried Infrastructure Facility, University of Birmingham, Birmingham* 02139, *UK*
[2]*Department of Earth Sciences, University of Turin, Via Tommaso Valperga Caluso,* 35, 10125 *Turin, Italy. E-mail: sergiocarmelo.vinciguerra@unito.it*
[3]*Institute of Geosciences, Johannes Gutenberg University, Mainz D-*55128, *Germany*
[4]*Department of Geology and Petroleum Geology, School of Geosciences, University of Aberdeen, King's College, Aberdeen AB*243*FX, UK*
[5]*Department of Earth, Atmospheric and Planetary Sciences, Massachusetts Institute of Technology, Cambridge, MA B*15 2*TT, USA*
[6]*Rock Mechanics Laboratory, School of Earth and Environmental Sciences, University of Portsmouth, Burnaby Building, Portsmouth PO*13*QL, UK*

Accepted 2023 February 25. Received 2023 February 11; in original form 2022 October 25

SUMMARY

Peak delays of acoustic emission (AE) data from rock deformation laboratory experiments are sensitive to both sample heterogeneities and deformation-induced impedance contrasts inside the sample. However, the relative importance of stochastic heterogeneity and discontinuities is uncertain, as is the relationship between peak delays and applied stress and strain. In the companion paper, we presented and analysed peak delay data from AE recorded in a sandstone sample that was triaxially deformed to failure. Here, we simulate *P–SV* waveforms of dominant frequency 200 kHz in a 2-D isotropic, layered medium using realistic parameters derived from the laboratory experiments previously analysed. Our aim is to provide a physical interpretation of the laboratory findings and constrain the role of a proxy of the evolving fault zone on peak delays. We consider a 2-D fault zone embedded in a host material that simulates the fracture plane as a more compliant layer and allows us to numerically investigate variations in peak delay. Measurements of background parameters, including isotropic velocity and fault thickness were optimized using laboratory data via an evolutionary algorithm. Our simulations clarify that near-source peak delay observations are sensitive to the heterogeneity within zones of intense strain even when far-field approximations are not valid. This sensitivity manifests through the arrival of trapped waves within the layer that is coupled with multiple reflections from the sample boundaries. Substantial uncertainties remain on the possibility of inverting sample parameters with 2-D simulations and such complex physics. Our combined experimental and modelling study suggests that peak delays and coda parameters are sensitive to the heterogeneity caused by faulting and strain variations at different stages of fault-inducing slow deformation.

Key words: Fracture and flow; Acoustic properties; Interface waves; Wave scattering and diffraction.

1 INTRODUCTION

Defined as the time lag between signal onset and the maximum amplitude arrival of the waveform, *peak delay* has been used to detect the complex effects of fault networks and fractured media on the scattering of seismic energy (e.g. Takahashi *et al.* 2007). Even when hypocentral distances are of the order of a few wavelengths and at the scale of heterogeneity (Napolitano *et al.* 2019), imaging with peak delay has become a standard method in volcanic settings, where lateral boundary conditions can disperse or trap much of the seismic energy, heavily affecting peak delay measurements that depend on frequency (De Siena *et al.* 2016, 2017; Gabrielli *et al.* 2020). Acoustic emission (AE), the laboratory analogue to seismic data (Benson *et al.* 2007), are used in our companion paper (King *et al.* 2022) to provide new insights into near-field processes that could affect parts of the waveforms where peak delays are measured (King *et al.* 2022). Analysis of waveform properties and the spatial distribution of high peak delays showed that the time-varying material properties of a developing fault zone likely played a key role in modifying energies. However, the physical process through which peak delays increased and how coda waves were formed during fault formation remained unclear.

Unveiling the dependence of peak delays on frequency and fault characteristics from the laboratory is challenging, with deformation experiments generally unable to reconstruct high-frequency amplitudes and late arrivals reliably. Depending on confining pressure and frequency, single or coalesced pores, microfractures of varying dimension (Pyrak-Nolte *et al.* 1990; Pyrak-Nolte & Nolte 1992; Frehner & Schmalholz 2010; Ekanem *et al.* 2014; Di Martino *et al.* 2021; Ma *et al.* 2022) and rheological heterogeneity (Ji & Wang 2011; Cionoiu *et al.* 2019) can all become significant scattering triggers for the seismic wavefield. Synthetic modelling is a viable way to reconstruct the features of the AE waveform and discern them from statistical heterogeneity as it allows the inclusion of both layers and statistical fluctuations in models while considering the spatial relation between source, localized heterogeneity and sample boundaries. Wave-equation finite-difference and spectral element methods can include these effects, targeting the evolution of peak delays through the coda as a marker of scattering (Di Martino et al 2022). Simulations can also naturally include anelasticity (e.g. Zhu & Carcione 2014) whilst considering many of the physical processes necessary to model attenuation measured from seismic waveforms in complex geological media.

In this second part of a two-part study, we model the 2-D propagation of *P–SV* waves to further investigate the experimental and mapping results presented in King *et al.* (2022). Observed waveforms from the laboratory experiment are used as a target to invert for time-dependent elastic moduli during the early phases of deformation and shortly following dynamic failure of the sample. The fault zone is modelled as a single isotropic layer embedded into an isotropic background medium, mimicking the distribution of deformation structure in the laboratory sample. In addition to the inserted layer, simulations consider the partial reflectivity of the finite boundary conditions and the dispersive properties of the deforming sample as essential elements of the AE waveform. The results provide new insight into relevant processes at the fault scale in the near-field.

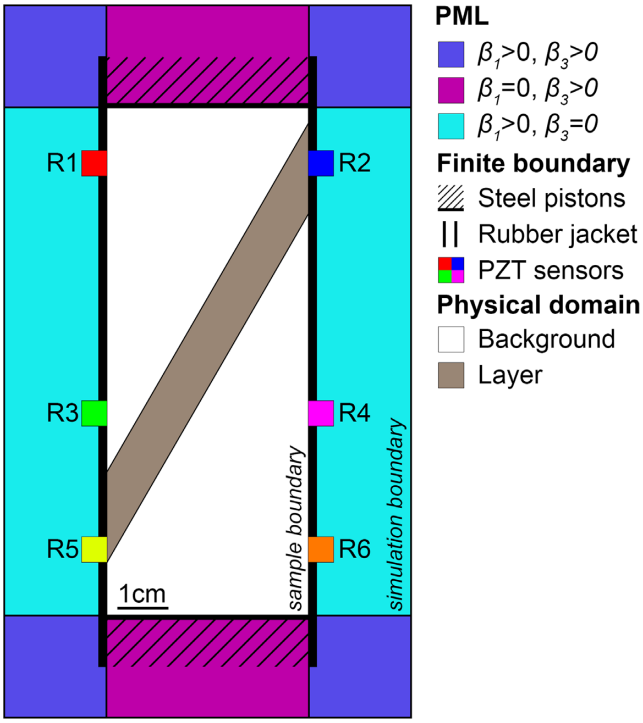

Figure 1. Implementation of the numerical model. Location parameters of the PML in axial (β_1) and radial (β_1) directions. Boundary conditions are independently constrained for steel piston and rubber jacket contacts. AE arriving to PZT located on the radial boundaries are modelled in the simulations for (a) a homogenous model and (b) a heterogenous model with an inserted layer.

2 NUMERICAL METHOD

The impact of developing heterogeneity that could lead to an increase in anisotropy of *P–SV* waveforms is modelled using the literature and data from the deformation experiment of Darley Dale Sandstone (DDS) described in the laboratory experiment. The 4×10 cm sample is deformed until dynamic failure under conventional triaxial conditions at a confining pressure of 20 MPa. An array of 1 MHz piezo-electric transducers (PZT) detects fracturing events as AE throughout the test. These sensors record the stress–displacement field as changes in the output voltage at a 10 MHz resolution. Please refer to King *et al.* (2022) for more details on the experimental setup and process.

We model isotropic viscoelastic *P–SV* waves in the *xz*-plane ($\mathbf{X} = [x, z]^T$) using the Kelvin–Voight model (e.g. Carcione *et al.* 2004). The simulations are solved with a 12th-order staggered finite-difference method in space and are second order in time. We consider three primary elements that best represent the main features of the laboratory sample under deformation to parametrize the numerical model (Fig. 1): (1) the background medium; (2) the finite boundary conditions of the sample edges (e.g. Yoshimitsu *et al.* 2016) and (3) an inserted layer of decreased stiffness that simulates the effect of a deforming zone of intense strain (Ji & Wang 2011). This three-layer model is not explicitly constrained from the laboratory experiment but is assumed as the dominant distribution of heterogeneity in the deformed sample. The sample-steel and sample-rubber boundaries are modelled as non-welded linear-slip surfaces with zero shear along the interface (Schoenberg. 1980; Far *et al.* 2014, Karmakar *et al.* 2023). To suppress the reflecting waves from the model boundary, we implement perfectly matched layers (PML–Collino & Tsogka 2001).

These elements are modelled with a grid step of 0.2 mm through 2-D spatial variations of the bulk modulus (K), shear modulus (G), density (ρ) and Q. Dispersive properties are modelled using Gaussian noise (per cent) of the elastic moduli (K, G, ρ) throughout the medium. When including random noise in the Q factor only (between 0 and 75 per cent), no appreciable differences in the synthetic waveforms were observed, although, this does not exclude the possibility of frequency-dependent velocities in the real data. This suggests that extrinsic attenuation did not play a major role at the frequencies investigated in the modelling and therefore it is unlikely it influenced parameter estimation. However, to reduce uncertainty and simplify the inversion, Q is fixed across the medium with the assumption that dispersion due to variations in scattering attenuation is dominant.

Initial source locations solved using a time difference of arrival method (King *et al.* 2020) are allowed to vary within a window of 2 cm to account for errors. Parameters are solved using a Covariance Matrix Adaptation Evolution Strategy (CMA-ES). This is a stochastic numerical optimization algorithm that is suited for ill-conditioned and noisy model spaces. The AE source is modelled as pure double-couple with a ricker wavelet of duration 0.01 ms

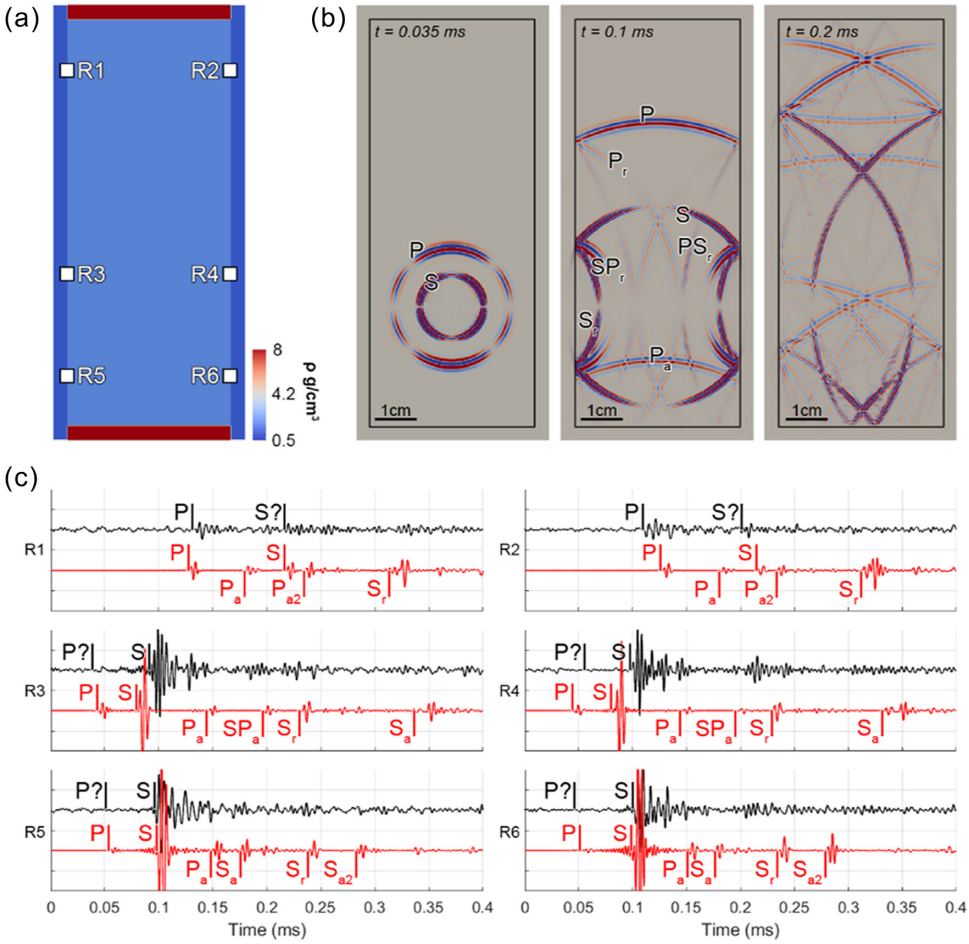

Figure 2. (a) Example density distribution for a non-dispersive medium. (b) *P–SV* wavefield snapshots of a simulated AE source. As time progresses multiple reflections and wave conversions occur due to interaction with axial (e.g. Pa) and radial (e.g. PSr) boundaries. (c) The wavefield is recorded at sensors R1 to R6. *P*- and *S*-wave arrival times for the modelled data (red) are shown together with observed data (black) from the laboratory experiment. Multiply reflected arrivals are observed to form the AE coda in the modelled data (labelled), although the fit to the observed data is poor.

and dominant frequency of 200 kHz, following the source characterization of King *et al.* (2021). The objective function is the weighted misfit between observed and modelled waveforms. The waveforms are normalized according to the average amplitude of the AE to minimize the effect of direction-dependent source amplitude variations (e.g. Kwiatek & Ben-Zion 2013) and bandpass filtered between 50 and 350 kHz prior to the misfit calculation. When solving for K and G, additional weighting is given towards periods of the signal that are increasing in amplitude to better fit arrival times. Conversely, when solving for dispersive properties, weighting is shifted towards periods of the signal that are decreasing in amplitude.

Modelling the dispersive nature of the waveform through Gaussian noise and an inserted layer leads to an inherently non-unique problem that is challenging to constrain. We thus follow an iterative approach whereby specific parameters of the model are fixed when solving for others. For example, elastic moduli (K, G, ρ) are fixed when solving for their associated Gaussian noise properties. Through investigation of the waveform, and the wider wavefield, this back-and-forth process allows us to make inferences on how the AE coda is formed and mitigates the need for more complex modelling.

3 RESULTS

The elastic moduli (K, G and Q) are estimated for the background medium using a non-dispersive model. To help constrain the inversion, ρ is set to 2300 kg m^{-3} and the boundary properties fixed to initial estimates for steel and rubber (Fig. 2a). Snapshots of the wavefield in the sample at $t = 0.035$, 0.1 and 0.2 ms show energy from an AE source that occurred before failure propagating outwards and interacting with the boundary of the sample (Fig. 2b). For a single source located in the lower half of the sample, bulk modulus, shear modulus and Q were solved by the inversion as 21.3 GPa, 15.6 GPa and 30, respectively. These values were independently verified by their fit to unsolved AE. Modelled waveforms shown are for particle velocities in the Z (vertical) direction (Fig. 2c). Shortly following source onset ($t = 0.035$ ms), the wavefield propagates with zero dispersion or scattering of the direct waves (P and S). For receivers located approximately at the same height as the source (R3 to R6), no P wave is detected in the laboratory data, although it is shown to arrive at ∼0.05 ms for those sensors in the simulation. The S wave arrives at ∼0.1 ms as the highest amplitude arrival. For receivers located above the source (R1 and R2), the P wave arrives at ∼0.11 ms and the S wave at ∼0.22 ms.

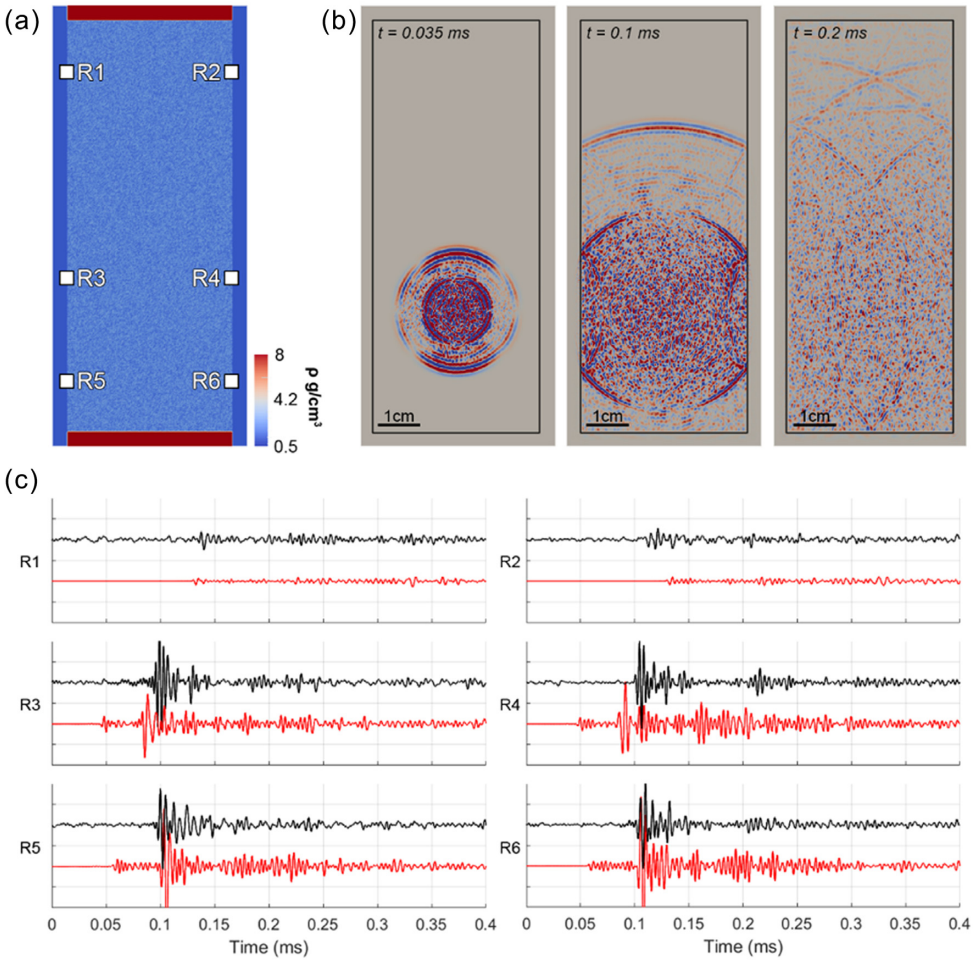

Figure 3. (a) Example density distribution for a dispersive medium using a Gaussian noise approximation. (b) Wavefield snapshots of the same simulated AE source shown in Fig. 2. (c) The wavefield recorded at sensors R1 to R6 demonstrates a more accurate fit of modelled (red) to observed (black) data when considering a dispersive background medium.

The snapshot at $t = 0.1$ ms highlights the rapid development of a complex wavefield driven by multiple reflections and the conversion of direct wave energies at the sample boundaries. As this model omits the third dimension, any boundary properties solved by this model are likely to be inaccurate, with the inversion compensating for missing amplitudes by increasing reflectivity. Whilst arrivals times of the *P* and *S* waves are considered reasonable within the known errors (i.e. source location), the fit of reflected phase arrivals in the coda is quite poor. This model cannot describe the 'tail' of the *S* wave in the observed data adequately (e.g. R5 at $t = 0.1$–0.15 ms) and leads to excessive amplitudes in the late coda (e.g. R2 at $t = 0.325$ ms) due to the coincident arrival of axial and radial reflections.

For a dispersive medium (Fig. 3a), snapshots of the wavefield (Fig. 3b) highlight strong scatter of source energy immediately following AE onset. At late lapse times (e.g. $t = 0.2$ ms), reflected phases are faintly visible in the noise. Taking the parameters solved in the previous model, dispersive properties for *K*, *G* and ρ were solved as ± 2, ± 1 and ± 2.5 per cent, respectively. Significant uncertainty still affects these values, which were dependent on each other and on the amplitude of boundary-reflected phases. Nonetheless, a better fit to the laboratory data is observed, for example, for the *S*-wave 'tail', now occurring in the modelled waveforms (Fig. 3c).

Fig. 4 simulates a similarly positioned AE source that occurred after sample failure. Background medium properties were set to those solved in the previous inversion. Layer properties were solved iteratively in successive inversions, with manual adjustment of layer thickness and position between each step. Elastic moduli (*K*, *G* and ρ) were solved as 14.1 GPa, 6.8 GPa and 2000 kg m^{-3} for an inserted layer of 8 mm thickness (Fig. 4a). Following source onset, the effect of the fault zone is observed as distortion of the AE wavefront at $t = 0.035$ ms due to slowing of the direct wave arrivals (Fig. 4b). At later lapse times (e.g. $t = 0.2$ ms), amplitudes remain high in the faulted area when compared to the background medium. To better fit later arrivals in the waveform coda, it was also necessary to reduce the reflectivity of the boundaries. A reasonable fit of the waveform data is observed for arrivals that directly interact with the fault zone (Fig. 4c). At R3, the direct *S*-wave arrival remains impulsive and is followed by high amplitudes that are rapidly cut-off at $t = 0.12$ ms. The latter arrivals tend to form from reflections between the fault zone and the boundary itself before being rapidly dispersed. For stations on the fault, for example, R5, the impulsiveness of the direct *S*-wave arrival is reduced, with an amplitude similar to that of the fault-boundary reflections that arrive shortly after. However, coda-wave amplitudes remain very high ($t >= 0.15$ ms), suggesting that the modelled fault zone is inaccurate when dispersing trapped

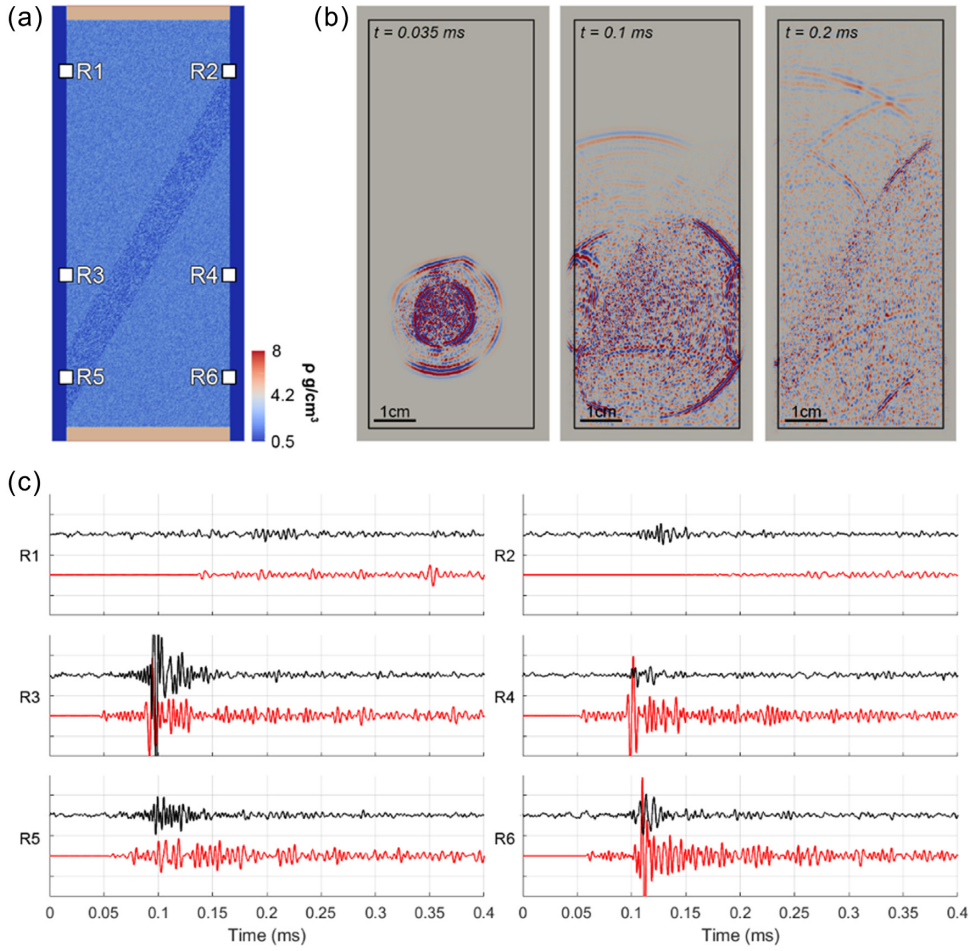

Figure 4. (a) Example density distribution for a faulted medium. (b) Wavefield snapshots of a simulated AE source. The effect of the fault zone is apparent from source onset with distortion of direct and reflected phase arrivals. Additional reflections are created by the fault zone itself. At late lapse times, high amplitudes are sustained within the fault zone. (c) Although it remains challenging to accurately fit observed (black) to modelled (red) data in the 2-D faulted medium, waveform broadening is evident for receivers in contact with the fault zone (e.g. R5).

energy. The fits of arrivals to the other sensors are generally poor, likely due to inadequate modelling of off-fault features.

For the same source shown in Fig. 4, elastic moduli describing the inserted layer are scaled linearly between properties of the background medium and their final value in order to investigate how the direct *S*-wave peak delay develops as the fault zone coalesces (Fig. 5). For energy that crosses and exits the fault zone (R3), there is a delay of up to 0.01 ms in the *S*-wave arrival time that corresponds to the gradual reduction in shear modulus and the time energy spent in the layer. This does not correspond to an increase in peak delay or significant modifications to amplitudes for those arrivals. For sensors located on or near to the fault zone (R5), there is a rapid reduction in direct *S*-wave amplitudes and a gradual broadening of the AE envelope as structure develops. This would lead to an increase in peak delay as the measurement would become more sensitive to the multiply reflected arrivals that arrive after the direct wave energy.

4 DISCUSSION

We have developed a model consisting of a layer of reduced elastic properties to characterize the development of damage within an isotropic homogeneous sample of DDS described in our companion paper (King *et al.* 2022) Models of scattering and absorption parameters for *P–SV* waveforms were obtained by fitting synthetic waveform data to observations from the laboratory experiment. The presented solutions were verified by their fit to unsolved AE. Our results show that the inclusion of time-dependent heterogeneity across the sample affects the delay of the maximum amplitudes of waveforms as a fault zone develops. Indeed, we observe propagation effects in the synthetic sample (where actual source-sensor distances are of the order of 3–7 wavelengths) even if far-field approximations are not applicable. The results thus support the use of peak delays, and more generally the early coda, as reliable measurements of attenuation by scattering beyond the Markov approximation (Napolitano *et al.* 2019; Zhang *et al.* 2021), and hint at the possibility of inferring fault properties from earthquake data.

The results presented in this study show that 3-D rheological heterogeneities (e.g. Cionoiu *et al.* 2019) and sample boundary conditions (e.g. Yoshimitsu *et al.* 2016) are required for an accurate description of AE waveform data. Neither of these features can be accurately reproduced with 2-D simulations, which affects the uncertainty in the estimation of fault properties. This resulted in poor fits to the amplitude and timing of reflected phase arrivals in the AE coda. Due to the unfeasibly high resolutions required

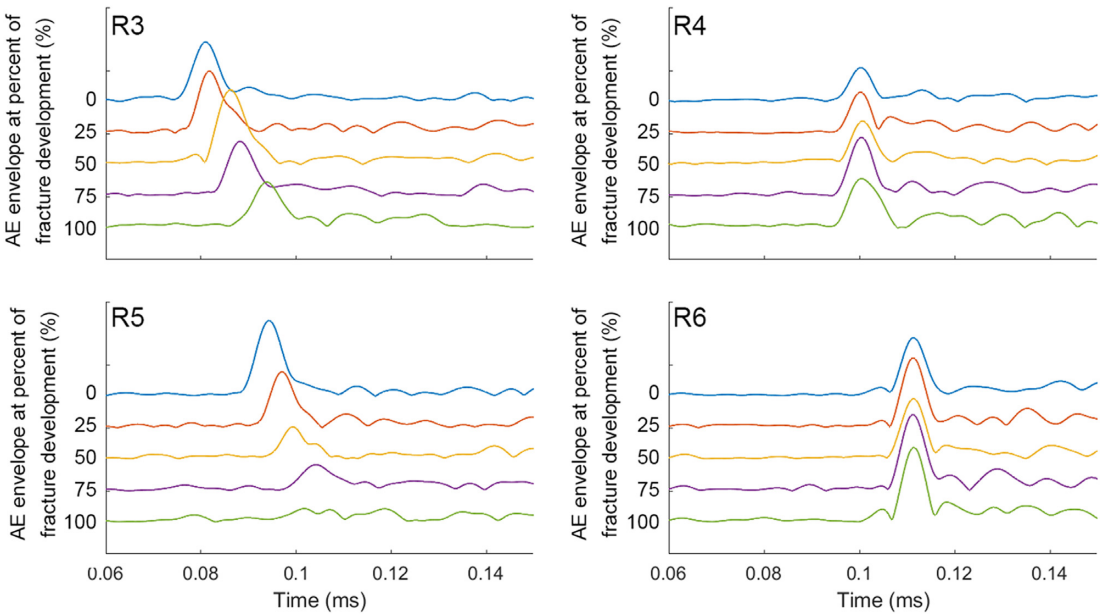

Figure 5. Elastic moduli that describe the fault zone are scaled linearly between the starting background medium properties and their final values to estimate the effect of a developing fracture on propagating AE. Energy that directly crosses the fault zone (e.g. R3) demonstrates a gradual decrease in direct *S*-wave velocities. For sensors located on or near to the fault zone (e.g. R5), peak amplitudes arrive later and become strongly diminished as the fracture develops. For energy that does not directly interact with the fault zone (e.g. R4 and R6), modifications to the direct wave are minimal.

to investigate details above 400 kHz we also need to neglect the frequencies that may better describe the fault zone. However, errors and limitations in the observed data proved to be the biggest hurdle, which has important implications on the understanding of the results shown in King *et al.* (2022).

The PZT used in the laboratory study are single-component radial sensors and are most sensitive to vertical particle motions. The *P–SV* model applied in this numerical study provided useful insight, highlighting the arrival of horizontally propagating *P*-wave energy that is not observed in the real data at sensors that are at the same height as the source. As the neural network strategy used for picking was unable to differentiate between *P*- and *S*-wave energy (King *et al.* 2020), the peak delay tomography is likely to include data from both (King *et al.* 2022, their fig. 7). To help address this problem, the laboratory study applied a CQT transform to target phases that arrive after the 'AE onset' (King *et al.* 2022, their fig. 2). The numerical simulations show that, at low frequencies, these arrivals are produced by the constructive interference of multiple-reflected phases arriving from the sample boundaries and the fault zone (e.g. Fig. 2c, R2). The first set arrives ∼0.1 ms and a second set at ∼0.225 ms after the AE onset (e.g. G2 and G3 in King *et al.* 2022, their fig. 6). At longer hypocentral distances (>6 cm), these waves can arrive together with the direct *S* wave, which does create some uncertainty in the peak delay measurement: however, these events are in the minority in the laboratory data. We therefore consider the low-frequency peak delay map to be dominantly a measurement of the slowing and broadening of reflected wave arrivals in the AE coda as they interact with the fault zone.

The proximity of the receiver location to the fault plays a significant role when considering delayed maximum amplitudes. In the numerical modelling, we observe a strong reduction in direct-wave amplitudes and an increase in the number of later arriving phases as heterogeneity increased for stations on the fault (e.g. Fig. 4, R5). Moreover, high energy scattering is sustained in the fault zone long after direct wave amplitudes have been dispersed (Fig. 4b). This result goes beyond a standard description of site effects, as it demonstrates the sensitivity of near-fault observations to the entire fault structure. Complex geology near the receiver can dominate seismic recordings, as demonstrated by field-scale investigations (Gabrielli *et al.* 2020; Qiu *et al.* 2020; Roy *et al.* 2020), laboratory measurements and modelling (Di Martino *et al.* 2021; 2022). Due to limitations of the presented simulations, we cannot explicitly verify data above 400 kHz, but our observations support the notion that the high frequency peak delay map is primarily the result of trapped and multiple-scattered waves dominating the envelope at receivers in contact with the highest heterogeneity.

The upscaling of these results has significant implications on the ability of seismic arrays to observe variations of fracturing and strain in faults with absorption and scattering. Observations and models support the ability of peak delays and absorption parameters to assess spatial changes of the Earth matrix in slow-deformation regimes, specifically fracture distribution and strain (Qiu *et al.* 2020). In this regime, high scattering and high absorption can identify the evolution of seismicity in active fault zones. Our results show that a combination of laboratory and synthetic modelling of fault zones is a powerful tool to understand properties of the Earth at the field scale.

5 CONCLUSIONS

AE data from rock deformation laboratory experiments on DDS are modelled to relate scattering and coda parameters to the evolving fault structure. Using numerically derived parameters bounded within a realistic range of measured observables, we demonstrate that modelling *P–SV* waves propagating in a heterogeneous sample can quantify the role of important seismic scattering attributes currently used at the field scale to map fault zones and understand their mechanics. The results depend on the relative geometry of sources, sensors and areas of strain. They provide benchmarks on: (1) the

ability of wave-propagation simulations to model seismic scattering and absorption parameters in rock deformation; (2) the onset of fault formation and the fracture growth, produced by the complex combination of on- and off-fault increase in microfracture volume; (3) the relevance of a simple peak delay or coda-attenuation analysis performed in tectonically active areas might have to measure fracturing, strain and rheological changes affecting in- and off-fault volumes and (4) the potential of these parameters to detect the stage of deformation and the geometry and size of fracture networks within the system.

Our results show that scattering- and absorption-dependent mapping are valid markers of fracture networks and deformation-induced heterogeneities, if not a possible failure-forecasting attribute outside the small-scattering regime currently in use at the field scale. The consequences of extended trapped signals within coda envelopes, generally considered comprised uniquely of stochastic scattered waves, challenge our ability to apply simple analytical techniques to near-field imaging. Particular attention should be given to the frequency and heterogeneity scales assumed by stochastic-based imaging techniques, including seismic interferometry, where trapped waves could have an unexpected central role.

ACKNOWLEDGMENTS

The first author would like to acknowledge the support from the DAFNI-ROSE grant (EP/V054082/1) that has provided access to the local HPC in the National Buried Infrastructure Facility (NBIF). The authors would also like to thank numerous reviewers, editors and members of the community for their valuable comments and feedback during the development of this research.

DATA AVAILABILITY

Acoustic emission data are obtained at the Rock Mechanics Laboratory, University of Portsmouth. Programming codes were developed in MATLAB ® version 2018a. Data and codes will be available upon reasonable request to the corresponding author.

REFERENCES

Benson, P.M., Thompson, B.D., Meredith, P.G., Vinciguerra, S. & Young, R.P., 2007. Imaging slow failure in triaxially deformed Etna basalt using 3D acoustic-emission location and X-ray computed tomography, *Geophys. Res. Lett.,* **34**(3), doi:10.1029/2006GL028721.

Carcione, J.M., Poletto, F. & Gei, D., 2004. 3-D wave simulation in anelastic media using the Kelvin–Voigt constitutive equation, *J. Comput. Phys.,* **196**(1), 282–297.

Cionoiu, S., Moulas, E. & Tajčmanová, L., 2019. impact of interseismic deformation on phase transformations and rock properties in subductions zone, *Sci. Rep.,* **9**(1), 1–6.

Collino, F. & Tsogka, C., 2001. Application of the perfectly matched absorbing layer model to the linear elastodynamic problem in anisotropic heterogeneous media, *Geophysics,* **66**(1), 294–307.

De Siena, L., Calvet, M., Watson, K.J., Jonkers, A.R.T. & Thomas, C., 2016. Seismic scattering and absorption mapping of debris flows, feeding paths, and tectonic units at Mount St. Helens volcano, *Earth planet. Sci. Lett.,* **442,** 21–31.

De Siena, L., Amoruso, A., Pezzo, E.D., Wakeford, Z., Castellano, M. & Crescentini, L., 2017. Space-weighted seismic attenuation mapping of the aseismic source of Campi Flegrei 1983–1984 unrest, *Geophys. Res. Lett.,* **44**(4), 1740–1748.

Di Martino, M.D.P., De Siena, L., Healy, D. & Vialle, S., 2021. Petromineralogical controls on coda attenuation in volcanic rock samples, *Geophys. J. Int.,* **226**(3), 1858–1872.

Di Martino, M.D.P., De Siena, L. & Tisato, N., 2022. Pore space topology controls ultrasonic waveforms in dry volcanic rocks, *Geophys. Res. Lett.,***49,** doi:10.1093/gji/ggab198.

Ekanem, A.M., Li, X.Y., Chapman, M., Ian, M. & Wei, J., 2014. Effect of fracture aperture on P-wave attenuation: a seismic physical modelling study, *ISRN Geophys.,* **2014,** 1–8.

Far, M.E., Jose, J.S., Robert, R.S., John, P.C., De-Hua, H. & Nikolay, D., 2014. Measurements of seismic anisotropy and fracture compliances in synthetic fractured Media, *Geophys. J. Int.,* **197**(3), 1845–1857.

Frehner, M. & Schmalholz, S.M., 2010. Finite-element simulations of Stoneley guided-wave reflection and scattering at the tips of fluid-filled fractures, *Geophysics,* **75**(2), T23–T36.

Gabrielli, S., De Siena, L., Napolitano, F. & Del Pezzo, E., 2020. Understanding seismic path biases and magmatic activity at Mount St Helens volcano before its 2004 eruption, *Geophys. J. Int.,* **222**(1), 169–188.

Ji, S. & Wang, Q., 2011. Interfacial friction-induced pressure and implications for the formation and preservation of intergranular coesite in metamorphic rocks, *J. Struct. Geol.,* **33**(2), 107–113.

Karmakar, S., Sahu, S.A. & Goyal, S., 2023. Reflection and refraction of plane wave at the junction of two dissimilar pre-stressed functionally graded piezothermoelastic media under different interfacial conditions, *Math. Mech. Solids.,* **28**(4), 891–919.

King, T., De Siena, L., Benson, P. & Vinciguerra, S., 2022. Mapping faults in the laboratory with seismic scattering 1: the laboratory perspective, *Geophys. J. Int.,* **232**(3), 1590–1599.

King, T., Benson, P., De Siena, L. & Vinciguerra, S., 2020. Acoustic emission waveform picking with time delay neural networks during rock deformation laboratory experiments, *Seismol. Res. Lett.,* **92,** 923–932.

King, T., Vinciguerra, S., Burgess, J., Benson, P. & Siena, L.D., 2021. Source mechanisms of laboratory earthquakes during fault nucleation and formation, *J. geophys. Res.: Solid Earth,* **126**(5), e2020JB021059. doi:10.1029/2020JB021059.

Kwiatek, G. & Ben-Zion, Y., 2013. Assessment of P and S wave energy radiated from very small shear-tensile seismic events in a deep South African mine, *J. geophys. Res.: Solid Earth,* **118**(7), 3630–3641.

Ma, R., Ba, J., Carcione, J.M. & Lebedev, M.(2022) P-wave scattering by randomly distributed aligned cracks in fractal media, *Geophys. J. Int.,* **229,** 900–914.

Napolitano, F., De Siena, L., Gervasi, A., Guerra, I., Scarpa, R. & La Rocca, M., 2019. Scattering and absorption imaging of a highly fractured fluid-filled seismogenetic volume in a region of slow deformation, *Geosci. Front*., **11,** 989–998.

Pyrak-Nolte, L.J. & Nolte, D.D., 1992. Frequency dependence of fracture stiffness, *Geophys. Res. Lett.,* **19**(3), 325–328.

Pyrak-Nolte, L.J., Myer, L.R. & Cook, N.G.W., 1990. Transmission of seismic waves across single natural fractures, *J. geophys. Res.,* **95**(B6), 8617. doi:10.1029/JB095iB06p08617.

Qiu, H., Allam, A.A., Lin, F.-C. & Ben-Zion, Y., 2020. Analysis of Fault zone resonance modes recorded by a dense seismic array across the San Jacinto Fault zone at Blackburn saddle, *J. geophys. Res.: Solid Earth,* **125**(10), e2020JB019756. doi:10.1029/2020JB019756.

Roy, N., Mukherjee, S. & Sahu, R.B., 2020. Influence of trapped soft/stiff soil layer in seismic site response analysis, *J. Earth Syst. Sci.,* **129**(1), 1–19.

Schoenberg, M., 1980. Elastic wave behavior across linear slip interfaces, *J. acoust. Soc. Am.,* **68**(5), 1516–1521.

Takahashi, T., Sato, H., Nishimura, T. & Obara, K., 2007. Strong inhomogeneity beneath quaternary volcanoes revealed from the peak delay analysis of S-wave seismograms of microearthquakes in northeastern Japan, *Geophys. J. Int.,* **168**(1), 90–99.

Yoshimitsu, N., Furumura, T. & Maeda, T., 2016. Geometric effect on a laboratory-scale wavefield inferred from a three-dimensional numerical simulation, *J. appl. Geophys.,* **132,** 184–192.

Zhang, T., Sens-Schönfelder, C. & Margerin, L., 2021. Sensitivity kernels for static and dynamic tomography of scattering and absorbing media with elastic waves: a probabilistic approach, *Geophys. J. Int.,* **225**(3), 1824–1853.

Zhu, T. & Carcione, J.M., 2014. Theory and modelling of constant-Q P- and S-waves using fractional spatial derivatives, *Geophys. J. Int.,* **196**(3), 1787–1795.